Changes in atmospheric eddy length with the seasonal cycle and global warming

by

Todd A. Mooring

Submitted to the Departments of Physics
and
Earth, Atmospheric and Planetary Sciences
in partial fulfillment of the requirements for the degrees of
Bachelor of Science in Physics
and
Bachelor of Science in Earth, Atmospheric and Planetary Sciences
at the
MASSACHUSETTS INSTITUTE OF TECHNOLOGY
June 2011

Author .....
Todd A. Mooring
Departments of Physics and
Earth, Atmospheric and Planetary Sciences
May 10, 2011

Certified by .....
Paul A. O'Gorman
Assistant Professor
Department of Earth, Atmospheric and Planetary Sciences
Thesis Supervisor

Accepted by .....
Nergis Mavalvala
Undergraduate Thesis Coordinator, Department of Physics

Accepted by .....
Samuel Bowring
Chair, Undergraduate Education Committee
Department of Earth, Atmospheric and Planetary Sciences

Changes in atmospheric eddy length with the seasonal cycle and global warming

by

Todd A. Mooring

Submitted to the Departments of Physics
and
Earth, Atmospheric and Planetary Sciences
on May 10, 2011, in partial fulfillment of the
requirements for the degrees of
Bachelor of Science in Physics
and
Bachelor of Science in Earth, Atmospheric and Planetary Sciences

Abstract

A recent article by Kidston et al. [8] demonstrates that the length of atmospheric eddies increases in simulations of future global warming. This thesis expands on Kidston et al.'s work with additional studies of eddy length in the NCEP2 reanalysis (a model-data synthesis that reconstructs past atmospheric circulation) and general circulation models (GCMs) from the Coupled Model Intercomparison Project phase 3. Eddy lengths are compared to computed values of the Rossby radius and the Rhines scale, which have been hypothesized to set the eddy length. The GCMs reproduce the seasonal variation in the eddy lengths seen in the reanalysis. To explore the effect of latent heating on the eddies, a modification to the static stability is used to calculate an effective Rossby radius. The effective Rossby radius is an improvement over the traditional dry Rossby radius in predicting the seasonal cycle of northern hemisphere eddy length, if the height scale used for calculation of the Rossby radius is the depth of the free troposphere. There is no improvement if the scale height is used instead of the free troposphere depth. However, both Rossby radii and the Rhines scale fail to explain the weaker seasonal cycle in southern hemisphere eddy length. In agreement with Kidson et al., the GCMs robustly project an increase in eddy length as the climate warms. The Rossby radii and Rhines scale are also generally projected to increase. Although it is not possible to state with confidence what process ultimately controls atmospheric eddy lengths, taken as a whole the results of this study increase confidence in the projection of future increases in eddy length.

Thesis Supervisor: Paul A. O'Gorman
Title: Assistant Professor

Acknowledgments

Many people contributed to the successful development of this thesis. Most of all I would like to thank Prof. Paul A. O'Gorman. He has been an excellent supervisor, from the moment I first walked into his office to inquire about UROP opportunities. He has always been available to answer my questions, listen to my ideas, and provide guidance about where the project should go next. I am proud to be the first person to complete a thesis under his supervision.

Thanks also to my mother, Mary Kay Quinlan, for proofreading the thesis and trying to help me manage my time. I hope I can successfully come up with a non-mathematical explanation for her of what this thesis is actually about.

Jane Connor read drafts of the thesis and made a key suggestion for organizing the introduction. Alessondra Springmann read drafts as well.

Last but certainly not least, I would like to acknowledge the MIT Undergraduate Research Opportunities Program's de Florez fund, which provided financial support during the summer of 2010.

Dedication

In loving memory of

Paul E. Quinlan

(1918-2010)

A wonderful grandfather

Contents

1 Introduction **15**

2 Eddy Scales **19**

2.1 Eddy length 19

2.2 Rossby radius 20

2.3 Rhines scale 22

3 Effective Static Stability **23**

3.1 Brief derivation 23

3.2 Seasonal cycle of asymmetry parameter λ 25

3.3 Seasonal cycle of static stability parameters 26

3.4 Effective Rossby radius 28

4 Results–Seasonal Cycle **31**

4.1 Northern hemisphere 32

4.2 Southern hemisphere 33

4.3 Causes of northern hemisphere seasonal cycle 33

5 Results–Global Warming **43**

5.1 Multimodel mean 43

5.2 Individual GCMs 45

6 Conclusion **53**

List of Figures

3-1 Seasonal cycles of asymmetry parameter λ 27

3-2 Seasonal cycles of dry and effective static stabilities 29

4-1 Northern hemisphere length scale seasonal cycles (1) 34

4-2 Northern hemisphere length scale seasonal cycles (2) 35

4-3 Southern hemisphere length scale seasonal cycles (1) 36

4-4 Southern hemisphere length scale seasonal cycles (2) 37

4-5 Components decomposition of L_{Reff} northern hemisphere seasonal cycle 40

4-6 Components decomposition of L_R northern hemisphere seasonal cycle 41

5-1 Fractional changes in L, L_R (WMO) and L_β over the 21st century . . 46

5-2 Fractional changes in L and L_{Reff} (WMO) over the 21st century . . . 47

5-3 Fractional changes in L, L_R and L_{Reff} (H) over the 21st century . . . 48

List of Tables

5.1 Fractional increases in eddy scales from 1981-2000 to 2081-2100 . . . 44

5.2 Quality of fit of $(\delta L_x/L_x, \delta L/L)$ points to lines $\delta L/L = \delta L_x/L_x$ . . . 51

Chapter 1

Introduction

Transient eddies are the central dynamical feature of the extratropical atmosphere. The eddies transport heat and moisture poleward and thus play a key role in the Earth's climate system [9]. An extensive body of work attempts to develop physical theories that explain the size of the eddies, which affects key aspects of their behavior such as propagation velocities and locations of dissipation [8, 22].

The eddies exist because the atmosphere is baroclinically unstable [21]. The archetypal models of baroclinic instability are those of Charney, Eady and Phillips [2, 3, 14]. The models demonstrate how certain types of perturbations to a zonally symmetric flow on an f- or β-plane can result in growing waves in the flow. The models yield predictions of the characteristic length scales of these waves [13, 22]. For all three, the characteristic length scale is

$$L_R \sim \frac{NH}{f}, \tag{1.1}$$

where L_R is referred to as the Rossby radius, N is the buoyancy frequency of the zonally symmetric flow, H is a relevant height scale, and f an appropriate value of the Coriolis parameter. The L_R of equation 1.1 is then identified with the scale of atmospheric eddies (e.g., [18]).

It has also been suggested that the eddy length is set by the fundamental physics of rotating stratified turbulence. Theory predicts that the energy of the turbulent

flow should cascade to larger spatial scales. If f varies in the rotating system, as it does for a planet or a β-plane, the inverse cascade can be stopped by the gradient in f, limiting the size of the eddies to

$$L_\beta \sim \left(\frac{v_{RMS}}{\beta}\right)^{1/2}. \tag{1.2}$$

L_β is referred to as the Rhines scale, v_{RMS} is the RMS velocity of the flow, and β is an appropriate value of df/dy [16, 22, 23].

Substantial debate exists in the literature on what sets the length scale of atmospheric eddies. Using simulations with a dry idealized GCM, Schneider and Walker (2006) [18] argue that the Rossby radius and the Rhines scale vary similarly as the pole-equator temperature gradient, planetary rotation rate and radius, and a convective lapse rate are adjusted. Both length scales yield reasonable predictions of the eddy length exhibited by the GCM, and Schneider and Walker further argue that there is not in fact an inverse energy cascade and so the eddy length is set by the Rossby radius. Merlis and Schneider (2009) [11] describe linear stability analyses of the zonal mean flows of many of the simulations presented in [18] and several related works, strengthening the connection between the growing waves of the baroclinic instability and observed atmospheric eddies by demonstrating that the Rossby radius also scales with the zonal length scale of the fastest-growing baroclinic waves.

Other studies suggest that the Rhines scale is the constraint on eddy lengths. Frierson et al. (2006) [6] adjust the amount of water vapor in the atmosphere of a moist idealized GCM and find that the Rhines scale is the best explanation of the resulting eddy lengths. Barry et al. (2002) [1] vary the pole-equator temperature gradient, planetary rotation rate and radius, radiative heating rate, and surface temperature in a moist GCM and calculate the eddy length, Rossby radius, and Rhines scale for each simulation. In this manner their study is similar to that of Schneider and Walker. However, Barry et al. find the Rhines scale to correlate better with the eddy length. The cause of the disagreement is unclear, but may relate to the substantial differences in the definition of eddy length between the two studies.

Furthermore, the idea that the Rossby radius as defined in equation 1.1 determines the eddy length scale of the real atmosphere suffers from a significant theoretical weakness. The dynamics of the real extratropical atmosphere are significantly influenced by latent heat release [17], but the baroclinic instability models from which the Rossby radius derives ignore this phenomenon. Studies of moist baroclinic instability (e.g.,[4, 5, 24]) suggest the need for modifications to equation 1.1 to include the effects of latent heating. Frierson et al. attempted to do so by making an ad hoc adjustment to N, but ultimately concluded that the Rhines scale was superior to this modified Rossby radius in accounting for the eddy lengths simulated by their GCM.

Any effect of latent heating on eddy lengths may depend on global temperatures, because of the rapid increase in saturation specific humidity with temperature [17]. Evidence that global warming will affect eddy lengths is provided by Kidston et al. (2010) [8], who analyze the output of 12 GCMs from the Coupled Model Intercomparison Project phase 3 [10]. Kidston et al. find that under the A2 emissions scenario, in which CO_2 levels reach approximately 820 ppm by 2100, eddy lengths increase in both hemispheres of each GCM studied. They argue that this process is linked to an increase in N, and use the NCEP/NCAR reanalysis to show that such an expansion of the eddies may already be occurring.

Recent work by O'Gorman (2011) [12] provides a path forward on the problem of modifying the Rossby radius to account for the effects of latent heating. O'Gorman derives a way to parameterize the latent heating effect with an adjustment to N, facilitating its addition to the calculation of the Rossby radius and other atmospheric dynamical quantities in which N is relevant. O'Gorman assesses the adjustment to N using simulations with a moist idealized GCM. Eddy lengths are found to increase with global temperatures, in agreement with Kidston, and the changes are predicted successfully by changes in the Rossby radius if the Rossby radius is calculated with the adjusted N. If the standard N is used, changes in the Rossby radius overestimate changes in the eddy length.

This thesis extends the work of Kidston and O'Gorman by using Rossby radii with and without the latent heating adjustment and the Rhines scale to analyze the future

changes in eddy length projected by six of the CMIP3 GCMs. Unlike the idealized GCMs used in most of the studies described above, the CMIP3 models have seasonal cycles. This permits calculations of the seasonal variation of the Rossby radii, Rhines scale, and eddy length in the simulated 20th century climate. Comparisons are made to the seasonal variations found in the NCEP-DOE Reanalysis 2 [7].

Chapter 2 of the thesis presents precise definitions of the eddy length, Rossby radius, and Rhines scale and explains how they were calculated from the GCM output and reanalysis. Chapter 3 reviews O'Gorman [12] to describe how the latent heating effect is taken into account via an effective static stability and presents details of the calculation of the effective static stability and the seasonal variation of static stability parameters. Chapters 4 and 5 present results on the variation of the eddy length, Rossby radii, and Rhines scale with the seasons and with global warming, respectively. Finally, conclusions are presented in chapter 6.

Chapter 2

Eddy Scales

The calculations presented in this thesis are based on the output of six coupled atmosphere-ocean GCMs (CSIRO-Mk3.5, ECHAM5/MPI-OM, GFDL-CM2.0, GFDL-CM2.1, INM-CM3.0, and MRI-CGCM2.3.2) from the Coupled Model Intercomparison Project phase 3 [10] and the NCEP-DOE Reanalysis 2 [7]. Characteristic values of the eddy length L, the Rossby radius L_R and the Rhines scale L_β were calculated for the latitude bands of 30-70 degrees in each hemisphere.

In the following discussion of how the various eddy scales were computed, a clear distinction must be drawn between zonal means and averages over latitude bands of finite width. The zonal and time mean of a quantity $(\cdot)$ will be denoted by $\overline{(\cdot)}$. The area-weighted time mean over latitudes $[\phi_{\min}, \phi_{\max}]$ is then

$$\langle(\cdot)\rangle = \frac{1}{\sin\phi_{\max} - \sin\phi_{\min}} \int_{\phi_{\min}}^{\phi_{\max}} \overline{(\cdot)} \cos\phi \, \mathrm{d}\phi. \tag{2.1}$$

2.1 Eddy length

A characteristic eddy length scale is defined using meridional winds at 300 hPa. To capture the transient eddies, daily-mean winds were filtered using a 13th-order high-pass Butterworth filter with a six-day cutoff to produce eddy meridional winds $v'(\phi, \chi)$ where ϕ is the latitude and χ is the longitude. At each latitude, the $v'(\phi, \chi)$ were Fourier transformed and squared to compute the energy in each zonal wave num-

ber and then time averaged to create a time-averaged eddy kinetic energy spectrum $\tilde{V}^2(\phi, k)$ where k is the zonal wavenumber.

At every latitude each zonal wavenumber can be associated with a local zonal wavelength

$$\Gamma(\phi, k) = \frac{2\pi a \cos\phi}{k}, \tag{2.2}$$

where a is the radius of the Earth. An eddy length is then computed over the full latitude band of integration by taking an energy- and area-weighted mean of the local zonal wavelengths

$$L = \frac{\langle \sum_{k=1}^{k_{max}} \Gamma(\phi, k)\tilde{V}^2(\phi, k)\rangle}{\langle \sum_{k=1}^{k_{max}} \tilde{V}^2(\phi, k)\rangle}. \tag{2.3}$$

2.2 Rossby radius

As discussed in the introduction, the Rossby radius is a characteristic length scale that emerges from the models of baroclinic instability of Charney, Eady, and Phillips [2, 3, 13, 14, 22]. It is convenient to express the terms on the right hand side of equation 1.1 in pressure coordinates, and similarly to Merlis and Schneider [11] and O'Gorman [12] the Rossby radius L_R will be defined

$$L_R = 2\pi \frac{\langle N^p \Delta p\rangle}{f}, \tag{2.4}$$

where N^p is a static stability parameter

$$N^p = \left(-\frac{1}{\overline{\rho}\overline{\theta}}\frac{\partial \overline{\theta}}{\partial p}\right)^{1/2}, \tag{2.5}$$

Δp is a relevant height scale in units of pressure, and f is an appropriate value of the Coriolis parameter. θ is the potential temperature and ρ is the density of the air, respectively.

As in Kidston et al. [8] and O'Gorman [12], N^p is evaluated in the lower troposphere (850-600 hPa) using zonal- and time-mean temperature and geopotential height fields. $\partial\overline{\theta}/\partial p$ was calculated using a finite difference between 850 and 600

hPa, while $\overline{\rho}$ and $\overline{\theta}$ are density-weighted vertical means. Aside from the convenience of consistency with previous studies, the 850-600 hPa region is a reasonable choice of evaluation level because it is a region where the growing baroclinic waves characterized by the Rossby radius have relatively large amplitudes [11]. There is some uncertainty about how to evaluate Δp. The Eady model of baroclinic instability features fixed walls at the top and bottom, and the upper wall can be identified with the tropopause [22]. Δp is then the free troposphere depth. The tropopause is diagnosed from temperature and relative humidity data using the WMO tropopause definition as the lowest level at which the lapse rate drops to 2 K km^{-1} and an algorithm similar to that given in [15]. (For computational simplicity, the WMO definition that the mean lapse rate between a putative tropopause and any point within 2 km above it not exceed 2 K km^{-1} has been slightly altered to require that the lapse rate at every level within 2 km above a putative tropopause be less than 2 K km^{-1}.) The free troposphere is assumed to begin at 850 hPa instead of the surface, to exclude the planetary boundary layer, and Δp is calculated as the difference between 850 hPa and the tropopause pressure. The issue of the vertical scale in the Charney model is more complex, but in one limiting case the vertical scale is the scale height [13]. In this case, it can be shown that Δp is equal to the mean value of the pressure in the levels being used to determine N^p. For the Phillips model, the height scale is the depth of the fluid, which can again be identified with the free troposphere depth [22].

The latitude for the evaluation of f was determined by identifying the maximum in the time-mean eddy meridional temperature transport

$$MTT_{eddy} = 2\pi a \overline{v'(\phi,\chi)T'(\phi,\chi)} \cos\phi, \tag{2.6}$$

where $T'(\phi,\chi)$ is the eddy temperature calculated by filtering daily-mean temperature fields with the same Butterworth filter used to determine $v'(\phi,\chi)$. To evaluate equation 2.6, $v'(\phi,\chi)$ and $T'(\phi,\chi)$ were computed at 850 hPa. Some calculations were

also done with f evaluated at a latitude ϕ_{MTT} given by

$$\phi_{\mathrm{MTT}} = \frac{\langle \phi \; v'(\phi,\chi) T'(\phi,\chi) \rangle}{\langle v'(\phi,\chi) T'(\phi,\chi) \rangle}, \tag{2.7}$$

where again $v'(\phi,\chi)$ and $T'(\phi,\chi)$ were evaluated at 850 hPa.

To evaluate equation 2.4, an area-weighted mean value of the numerator $\langle N^p \Delta p \rangle$ is computed over the 30-70 degree integration region and then divided by f evaluated at the latitude with the maximum value of MTT_{eddy} or at ϕ_{MTT}.

2.3 Rhines scale

The Rhines scale [16, 22, 23] is defined by

$$L_\beta = \frac{(\langle v'^2 \rangle)^{1/4}}{(\beta)^{1/2}}, \tag{2.8}$$

where $\langle v'^2 \rangle$ is a time and spatial mean over the region in question of the eddy kinetic energy $v'^2(\phi,\chi)$ at 300 hPa and β is evaluated at some appropriate latitude. β is evaluated at the latitude of the maximum in

$$EKE = \overline{v'^2(\phi,\chi)} \cos\phi, \tag{2.9}$$

where EKE is proportional to the area-weighted eddy kinetic energy.

Chapter 3

Effective Static Stability

O'Gorman's addition [12] of the effects of latent heat release to large-scale dry-atmosphere dynamical theories, such as baroclinic instability problems, is accomplished by replacing the traditional dry static stability where it appears in such theories with an appropriately-defined effective static stability. This chapter reviews the derivation of the effective static stability and analyzes the seasonal cycle of an asymmetry parameter λ that is invoked in the derivation. It then discusses the seasonal cycles of the dry static stability parameter N^p and its moist counterpart N^p_{eff} and concludes by formally presenting the definition of an eddy scale L_{Reff}, a Rossby radius evaluated using the effective static stability.

3.1 Brief derivation

The full derivation of the effective static stability is given in [12] and will not be reiterated here. In summary, it involves consideration of the changes in dry potential temperature θ and equivalent potential temperature θ^* of a saturated air parcel. If diabatic heating and cooling are ignored, θ^* will be conserved following the parcel's motion and thus

$$\frac{D\theta}{Dt} = H(-\omega)\omega \left.\frac{\partial\theta}{\partial p}\right|_{\theta^*} = \omega^{\uparrow} \left.\frac{\partial\theta}{\partial p}\right|_{\theta^*}, \tag{3.1}$$

where $H(\cdot)$ denotes the Heaviside step function, $\omega = Dp/Dt$ is the vertical pressure velocity, $\omega^{\uparrow} = H(-\omega)\omega$, and the θ^* subscript on the partial derivative indicates that the partial derivative is taken at constant θ^*. The Heaviside step function appears because condensation and latent heat release are being approximated as occurring always and only when the parcel ascends.

For purposes of this derivation, eddy quantities will be defined as departures from the zonal mean and denoted $(\cdot)'$. Denoting a zonal mean at fixed time by $\overline{\overline{(\cdot)}}$, it can thus be shown that

$$\frac{\partial \theta'}{\partial t} = -\omega' \frac{\partial \overline{\overline{\theta}}}{\partial p} + \omega^{\uparrow\prime} \left. \frac{\partial \overline{\overline{\theta}}}{\partial p} \right|_{\theta^*}, \tag{3.2}$$

if the partial derivatives of θ' with respect to pressure are set to zero. It is easy to see that the first term of this equation is associated with the advection of dry air through the point at which the equation is evaluated, while the second term comes from latent heat release in rising air. In a dry atmosphere, this second term would disappear.

The effective disappearance of the second term of equation 3.2 in the real moist atmosphere can be achieved by folding it into the first term. This is accomplished by writing

$$\omega^{\uparrow\prime} = \lambda \omega' + \epsilon, \tag{3.3}$$

where λ is a constant that is regressed for using ω' and $\omega^{\uparrow\prime}$ taken from GCM output or reanalysis. Then, taking $\omega^{\uparrow\prime} \approx \lambda \omega'$, equation 3.2 can be rewritten

$$\frac{\partial \theta'}{\partial t} = \omega' \left[-\frac{\partial \overline{\overline{\theta}}}{\partial p} + \lambda \left. \frac{\partial \overline{\overline{\theta}}}{\partial p} \right|_{\theta^*} \right]. \tag{3.4}$$

The quantity in brackets in equation 3.4 is defined as the effective static stability

$$-\left. \frac{\partial \overline{\overline{\theta}}}{\partial p} \right|_{\text{eff}} = -\frac{\partial \overline{\overline{\theta}}}{\partial p} + \lambda \left. \frac{\partial \overline{\overline{\theta}}}{\partial p} \right|_{\theta^*}. \tag{3.5}$$

λ is related to the up-down asymmetry of the eddy vertical velocity field, so it will be referred to as an asymmetry parameter.

When equation 3.5 is substituted into equation 3.4, equation 3.4 acquires the same functional form as the dry-atmosphere version of equation 3.2. Thus the effects of latent heating can be parameterized by substituting $-\partial\theta/\partial p|_{\text{eff}}$ for $-\partial\theta/\partial p$ wherever the latter appears. Because saturated air moving upwards is warmed by latent heat release, $\partial\theta/\partial p|_{\theta^*} < 0$ and so the effect of latent heating is to reduce the effective static stability of the atmosphere relative to the dry value.

3.2 Seasonal cycle of asymmetry parameter λ

The value of the effective static stability as a conceptual tool for analyzing moist atmospheric circulations is partially dependent on λ remaining relatively constant with the seasonal cycle and with global climate change. Although O'Gorman [12] notes that some previous works on moist baroclinic instability ([4, 5, 24]) imply $\lambda \to 1$ with the increasing specific humidity that would occur with global warming, idealized GCM simulations presented in that study nevertheless suggest a λ largely independent of temperatures.

Using the output of the idealized GCM, O'Gorman [12] calculated average values of λ over the full areal and vertical extent of the extratropical troposphere. They changed by just 0.02 (from 0.59 to 0.61) as the GCM's global mean surface temperature was increased from 270 to 316 K. However, the idealized GCM has simplified parameterizations, a global mixed layer ocean as the lower boundary, and no seasonal or diurnal cycles. The constancy of λ in more realistic models of the climate system and the real world as represented in NCEP2 is thus worth investigating.

Evaluation of λ requires ω data at high temporal resolution. The monthly-mean values archived in the CMIP3 dataset are inadequate for this purpose, so λ was evaluated only for NCEP2, using 4x daily ω data for 1981-2000. It can be shown that at a single time, latitude, and pressure level

$$\lambda = \frac{\overline{\overline{\omega\omega^{\uparrow}}} - \overline{\overline{\omega}}\,\overline{\overline{\omega^{\uparrow}}}}{\overline{\overline{\omega^2}} - \overline{\overline{\omega}}^2}, \tag{3.6}$$

and for simplicity the time-mean λ is evaluated using the approximate equation

$$\lambda \approx \frac{\overline{\omega\omega^{\uparrow}} - \overline{\omega}\,\overline{\omega^{\uparrow}}}{\overline{\omega^2} - \overline{\omega}^2}. \tag{3.7}$$

After computing λ as a function of latitude and pressure for each month, monthly regional mean values $\langle\lambda\rangle$ over 30-70 degrees in each hemisphere were calculated using λ values at 850, 700, and 600 hPa. Several additional calculations also took mass-weighted depth averages of λ over 1000-300, 1000-200, and 1000-100 hPa, for more direct comparability to the idealized GCM results. The resulting seasonal cycles of λ are presented in Fig. 3-1. Although the amplitudes of the seasonal cycles in these hemispherically-averaged λ values are comparable to the change in the idealized GCM's annual mean λ over a very large range of global temperatures, it can be shown that these variations are still small enough to approximate λ in all seasons and both regions by the average of the two regional annual mean values of λ at 700 hPa. It is interesting to note that λ values peak during the winter and are minimized during the summer. This is the opposite of what would occur if the regionally-averaged λ values were increasing functions of regional-mean temperatures, as one might expect based on the temperature dependence of λ documented in [12].

3.3 Seasonal cycle of static stability parameters

Because λ is apparently adequately stable over the seasonal cycle and with a changing climate, the effective static stability can be readily used to parameterize the effect of latent heating on atmospheric eddies. As a complement to the traditional dry static stability parameter N^p defined in equation 2.5, it is possible to define an effective static stability parameter

$$N^p_{\text{eff}} = \left(-\frac{1}{\overline{\rho}\overline{\theta}}\left.\frac{\partial\overline{\theta}}{\partial p}\right|_{\text{eff}}\right)^{1/2} = \left(-\frac{1}{\overline{\rho}\overline{\theta}}\left[\frac{\partial\overline{\theta}}{\partial p} - \lambda\left.\frac{\partial\overline{\theta}}{\partial p}\right|_{\theta^*}\right]\right)^{1/2}, \tag{3.8}$$

where the zonal means at fixed time in equation 3.5 have been replaced by zonal and time means.

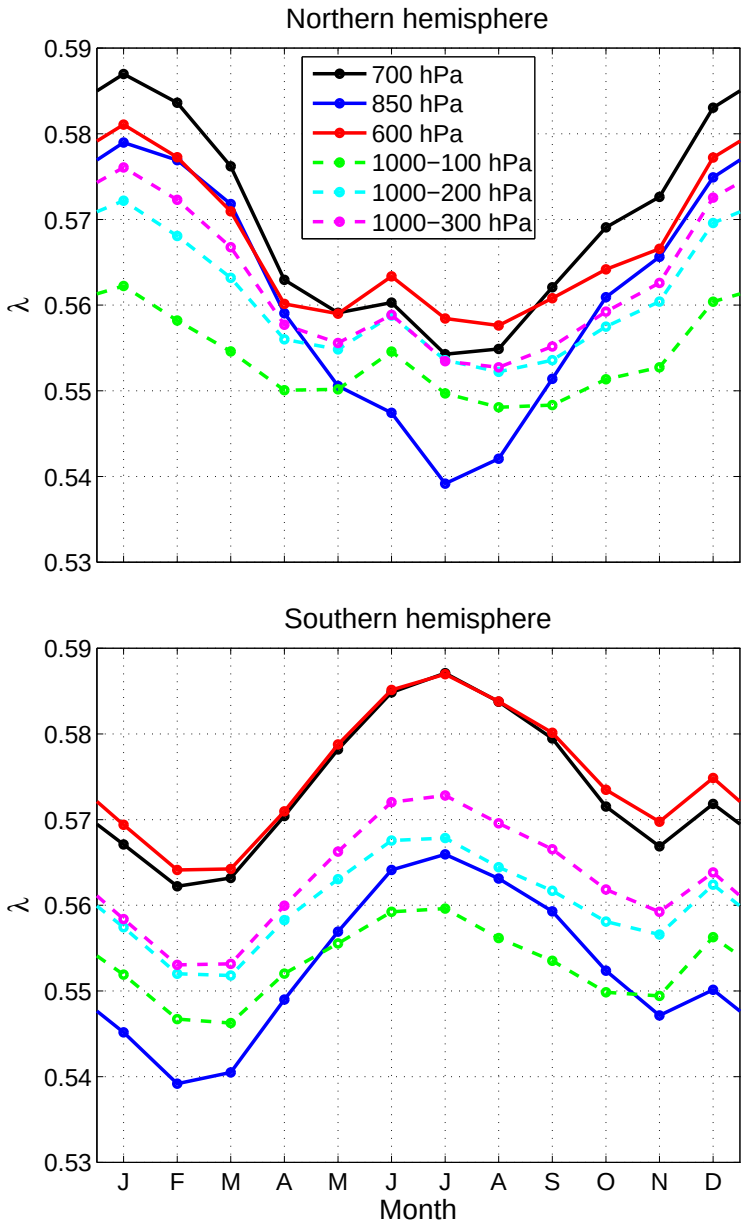

Figure 3-1: The seasonal cycles of λ computed using 30-70 degrees in each hemisphere and various levels of the atmosphere. The underlying 4x daily ω data was taken from the 1981-2000 subset of the NCEP2 reanalysis. Clear seasonal cycles are present for all methods of λ evaluation, although depth averaging tends to reduce the cycle amplitude. Values of λ were not available at 1000 hPa for every latitude. Although the depth averages list 1000 hPa as the bottom of the integration region for both hemispheres, the integration extended only as far down as 925 hPa in the northern hemisphere. In the southern hemisphere, 1000 hPa λ values were available for 30-50 degrees S in most months. At 70 degrees S, λ was unavailable at 925 hPa and the vertical integration was stopped at 850 hPa.

To investigate the importance of the latent heating effect, $\langle N^p \rangle$ and $\langle N^p_{\text{eff}} \rangle$ were computed for each calendar month and GCM/reanalysis using data from latitudes 30-70 degrees in each hemisphere and years 1981-2000. Rather than analyzing each of the six CMIP3 GCMs individually, the monthly values for each GCM were averaged to form multimodel monthly means. The NCEP2 reanalysis was not included in the means and was studied separately.

The seasonal cycles of $\langle N^p \rangle$ and $\langle N^p_{\text{eff}} \rangle$ are plotted in Fig. 3-2. The multimodel mean and NCEP2 seasonal cycles are similar in nearly every respect. In both hemispheres, the effective static stability parameter is clearly smaller than its dry counterpart. In the northern hemisphere, the inclusion of the latent heating effect substantially increases the amplitude of the seasonal cycle in both absolute and fractional senses and alters its phase. In contrast, the absolute amplitude of the southern hemisphere seasonal cycle is reduced. The substantial differences between $\langle N^p \rangle$ and $\langle N^p_{\text{eff}} \rangle$ suggest a significant influence of latent heat release on the behavior of the midlatitude atmosphere.

3.4 Effective Rossby radius

N^p_{eff} can be used to calculate an effective Rossby radius, defined in analogy to equation 2.4 as

$$L_{\text{Reff}} = 2\pi \frac{\langle N^p_{\text{eff}} \Delta p \rangle}{f}. \tag{3.9}$$

As in the definition of the dry Rossby radius (equation 2.4), $\overline{\rho}$, $\overline{\theta}$, and the pressure derivatives of potential temperature in equation 3.8 were evaluated using data from 850-600 hPa. λ was evaluated at 700 hPa. The latitude of f evaluation was found using the same methods as for L_R. Equation 3.9 was evaluated by finding $\langle N^p_{\text{eff}} \Delta p \rangle$ over 30-70 degrees in the hemisphere of interest, the same integration region used for the eddy scales described in chapter 2.

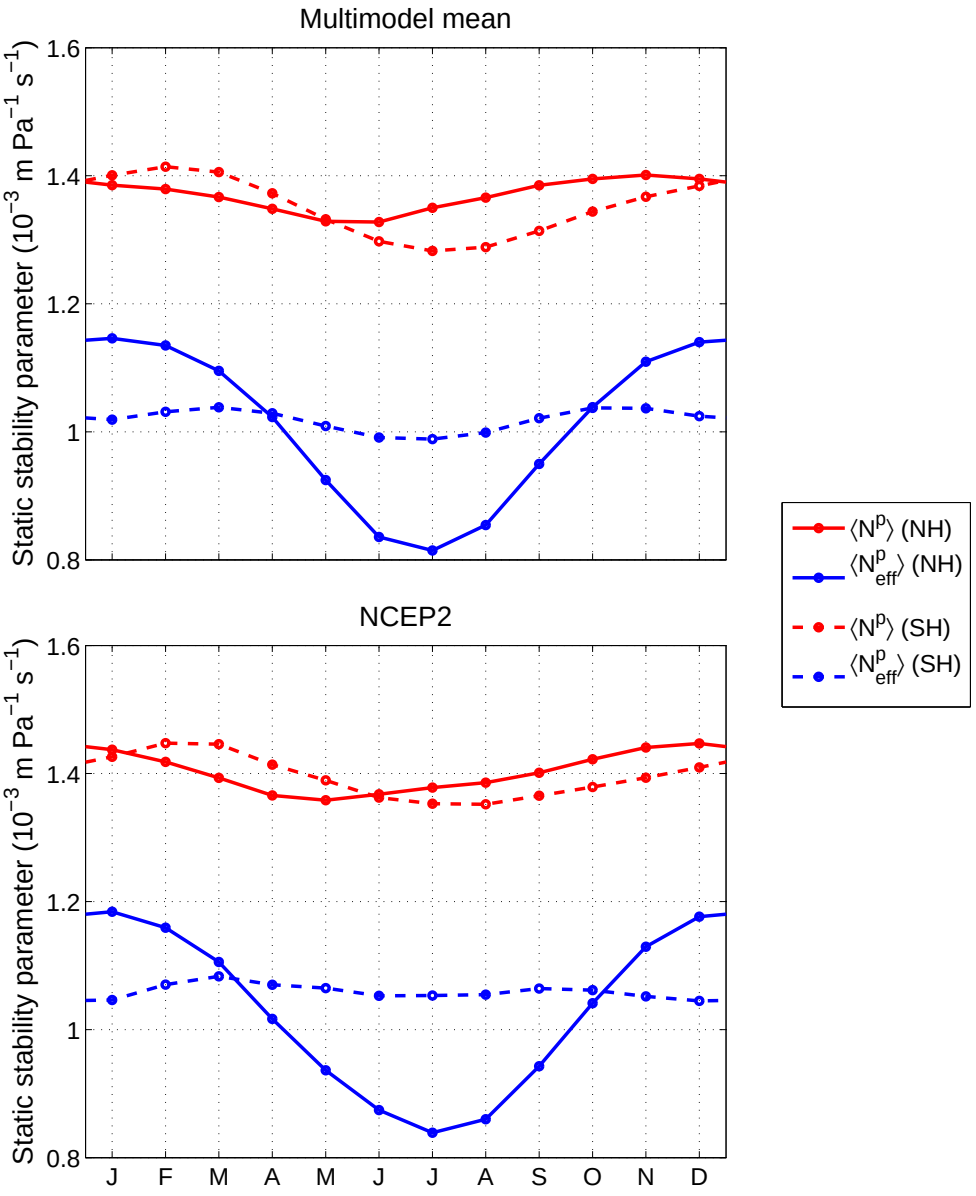

Figure 3-2: $\langle N^p \rangle$ and $\langle N^p_{\text{eff}} \rangle$ are displayed for both hemispheres in each panel. Solid lines indicate quantities evaluated using 30-70 degrees N, while dashed lines indicate quantities evaluated using 30-70 degrees S. In both hemispheres the effective static stability is reduced substantially relative to the dry static stability. $\langle N^p \rangle$ and $\langle N^p_{\text{eff}} \rangle$ were calculated using temperature and geopotential height fields from 850-600 hPa, and λ was evaluated at 700 hPa.

Chapter 4

Results–Seasonal Cycle

The studies reviewed in chapter 1 analyze eddy scales in idealized GCMs in which parameters are varied, or changes in annual mean eddy lengths in more realistic GCMs and reanalysis. None of the idealized GCMs included a seasonal cycle. Accordingly, analysis of the seasonal variability of the eddy scales described in chapters 2 and 3 may provide additional information about the physical causes of observed and modeled eddy lengths. The northern and southern hemispheres will be discussed separately, because of substantial qualitative differences in both the character of the eddy length seasonal cycles and the success of the various Rossby radii and the Rhines scale in predicting the cycles.

As in chapter 3, a mean value of each eddy scale was determined for each calendar month and GCM/reanalysis using data from 1981-2000. The monthly values for each GCM were averaged into multimodel monthly means, while the NCEP2 results were kept separate.

The L_R, L_{Reff}, and L_β described in chapters 2 and 3 can be thought of as predictions of the eddy length L. However, the underlying theories predict the existence of unstable waves of a range of wavelengths and so cannot be interpreted as yielding particular exact values for L. Accordingly, the Rossby radii and Rhines scale seasonal cycles were all rescaled for the best fit to the L seasonal cycle before making any comparisons.

For analytical purposes, it was assumed that the actual eddy length L and a

theoretical characteristic length scale L_x, where L_x is one of the Rossby radii or the Rhines scale, were related by a rescaling constant c such that $L = cL_x$. It can be shown that the least-squares best-fit value of c is given by

$$c = \frac{\sum_{i=1}^{12} L^i L_x^i}{\sum_{i=1}^{12} (L_x^i)^2}, \tag{4.1}$$

where i indexes over months. c was evaluated separately for each L_x and hemisphere.

4.1 Northern hemisphere

The seasonal cycles of eddy length, various Rossby radii, and the Rhines scale for the northern hemisphere are displayed in Figs. 4-1 and 4-2. The Rossby radii and Rhines scale have been rescaled for the best fit to the eddy length seasonal cycle as described above. The multimodel mean of the GCM eddy lengths exhibits a distinct seasonal cycle, with the eddies at their longest in the northern hemisphere winter. The multimodel mean eddy length seasonal cycle compares favorably with the eddy length seasonal cycle in the NCEP2 reanalysis, and indeed the qualitative relationships among all seasonal cycles plotted are basically the same for both the multimodel mean and NCEP2. This suggests a remarkable degree of success by the GCMs in reproducing observed seasonal variations in atmospheric eddy activity.

In Fig. 4-1, the seasonal cycles of both L_{Reff} and L_β are qualitatively quite similar to the L seasonal cycle. The amplitude of the L_{Reff} cycles is somewhat too large, although this overestimate is reduced by the use of ϕ_{MTT} instead of the latitude of the maximum in MTT_{eddy} for the evaluation of f. In contrast, the amplitude of the L_β seasonal cycle is too small. L_β is also notably too constant in January-April. Agreement of the L_R seasonal cycles with the L seasonal cycle is less impressive, particularly if the ϕ_{MTT} method of selecting the f evaluation latitude is used.

Fig. 4-2 displays a number of the same seasonal cycles as Fig. 4-1 but shows seasonal cycles of L_R and L_{Reff} with Δp identified as the scale height of the atmosphere instead of the free troposphere depth. Pursuant to the discussion in section 2.2, Δp

is taken as 725 hPa. However, this choice does not actually matter because since Δp does not change with the seasons, it is essentially an arbitrary constant factor whose effects will be eliminated by the rescaling that is applied before plotting.

The principal conclusion to be drawn from Fig. 4-2 is that the use of the scale height in place of the free troposphere depth as the value of Δp in Rossby radius calculations increases the amplitude of the rescaled seasonal cycle. In contrast to the results displayed in Fig. 4-1, this choice results in L_R being a comparable or better fit to the eddy length seasonal cycle than L_{Reff}.

4.2 Southern hemisphere

Figs. 4-3 and 4-4 display eddy length, Rossby radii, and Rhines scale seasonal cycles for the southern hemisphere. Both the multimodel mean and NCEP2 seasonal cycles are again similar, although the cycles themselves are strikingly different from their northern hemisphere counterparts. The annual mean eddy length is noticeably larger, and its seasonal cycle amplitude is smaller. Additionally, the eddy length seasonal cycle is no longer generally sinusoidal in shape.

Unlike in the northern hemisphere, none of the Rossby radii or Rhines scale seasonal cycles appear to succeed in explaining the eddy length seasonal cycle. Although the rescaled Rossby radius and Rhines scale cycles have reasonable amplitudes, they are not able to reproduce the January-February minima and September-October maxima that characterize the eddy length seasonal cycle. The choice of the free troposphere depth or the scale height for Δp makes little difference to the Rossby radii seasonal cycles.

4.3 Causes of northern hemisphere seasonal cycle

To study the causes of the seasonal cycle in eddy length, the seasonal cycles of the dry and effective Rossby radii plotted in Figs. 4-1 and 4-2 were decomposed into their components. Only results from the northern hemisphere are presented, as the failure

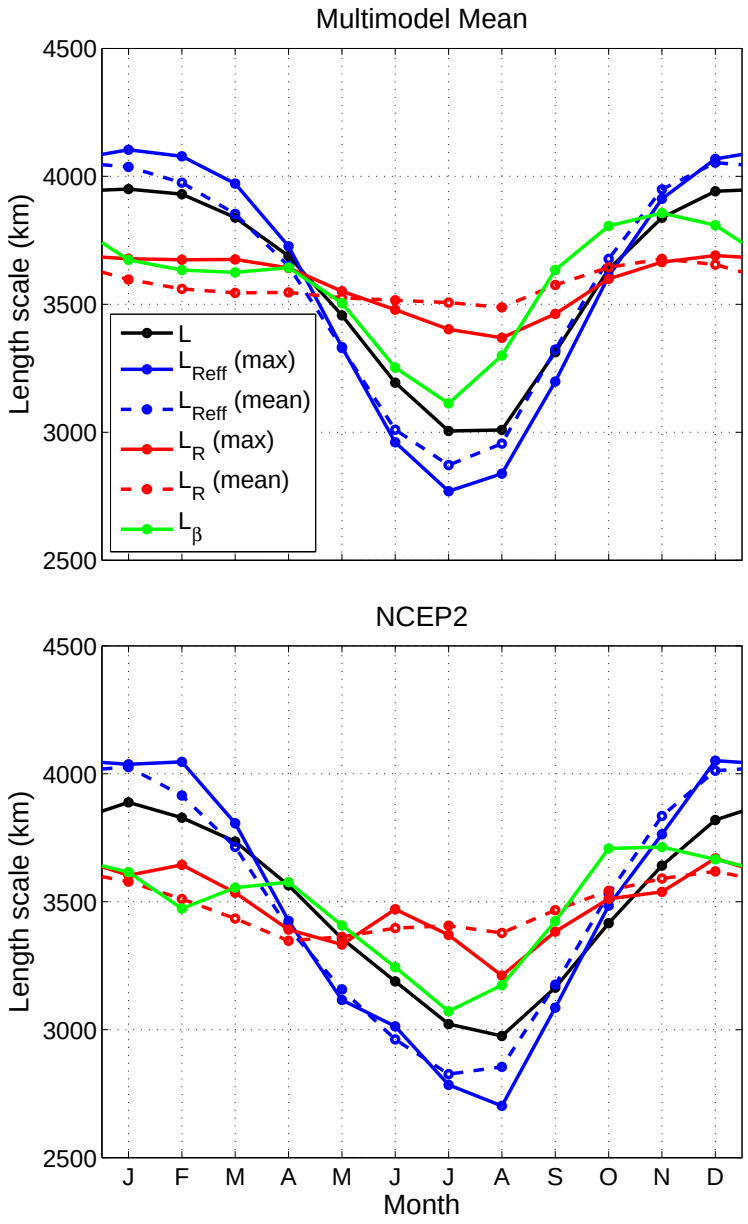

Figure 4-1: Seasonal cycles of eddy length, various dry and effective Rossby radii, and the Rhines scale over 30-70 degrees N during 1981-2000. The Rossby radii labeled (max) had f evaluated at the latitude of the maximum in MTT_{eddy} defined in equation 2.6. Rossby radii labeled (mean) had f evaluated at ϕ_{MTT} as defined in equation 2.7. MTT_{eddy} and ϕ_{MTT} were evaluated at 850 hPa, and the free troposphere depth was used as Δp. For the Rhines scale, β was evaluated at the latitude of the maximum in EKE (equation 2.9).

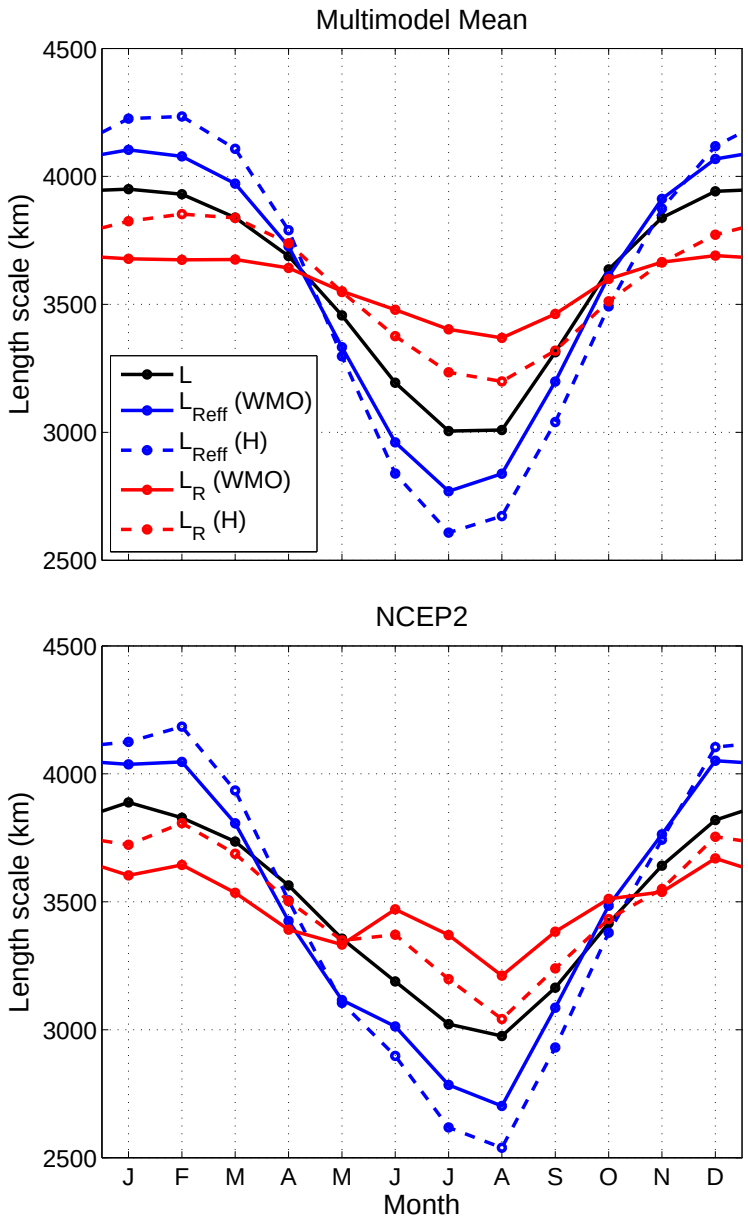

Figure 4-2: Seasonal cycles of eddy length and various dry and effective Rossby radii over 30-70 degrees N during 1981-2000. The Rossby radii labeled (WMO) had the height scale Δp in equation 2.4 or 3.9 defined as the free troposphere depth. Rossby radii labeled (H) had Δp identified as the scale height. In all cases f was calculated at the latitude of the maximum in MTT_{eddy}, evaluated at 850 hPa.

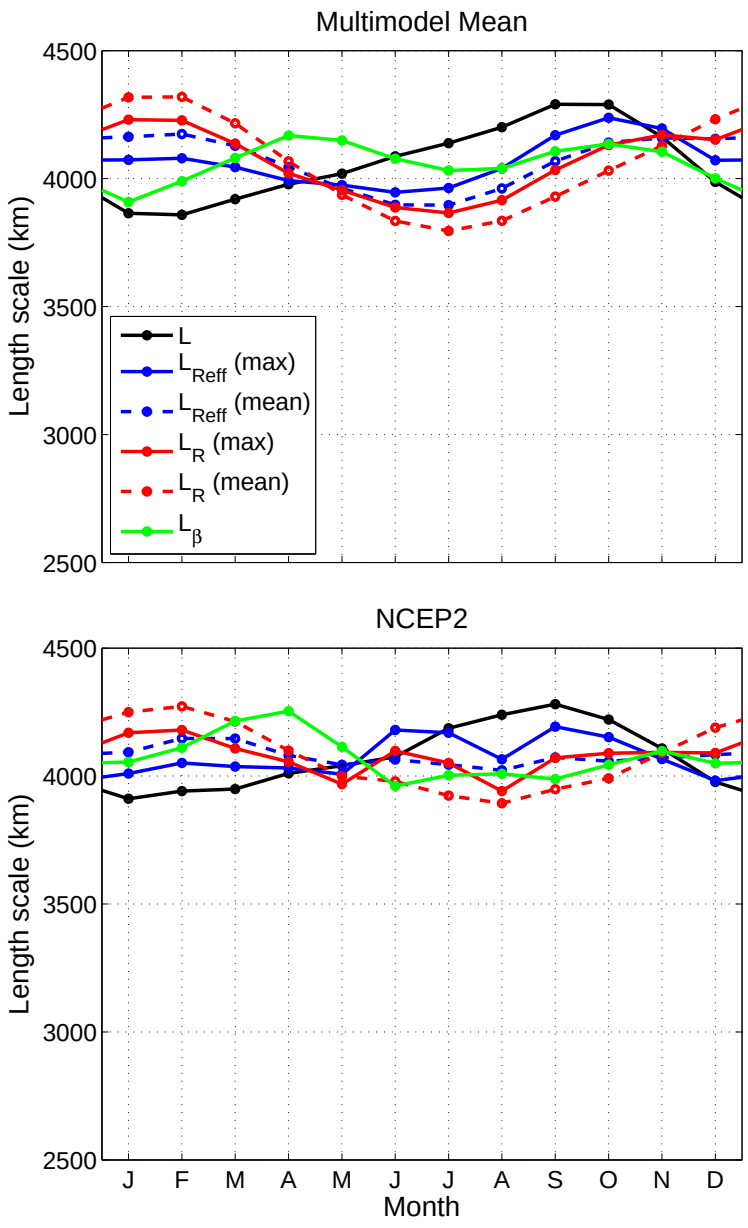

Figure 4-3: Seasonal cycles of eddy length, various dry and effective Rossby radii, and the Rhines scale over 30-70 degrees S during 1981-2000. The Rossby radii labeled (max) had f evaluated at the latitude of the maximum in MTT_{eddy}. Rossby radii labeled (mean) had f evaluated at ϕ_{MTT}. Both MTT_{eddy} and ϕ_{MTT} were calculated at 850 hPa, and the free troposphere depth was used as Δp. For the Rhines scale, β was evaluated at the latitude of the maximum in EKE.

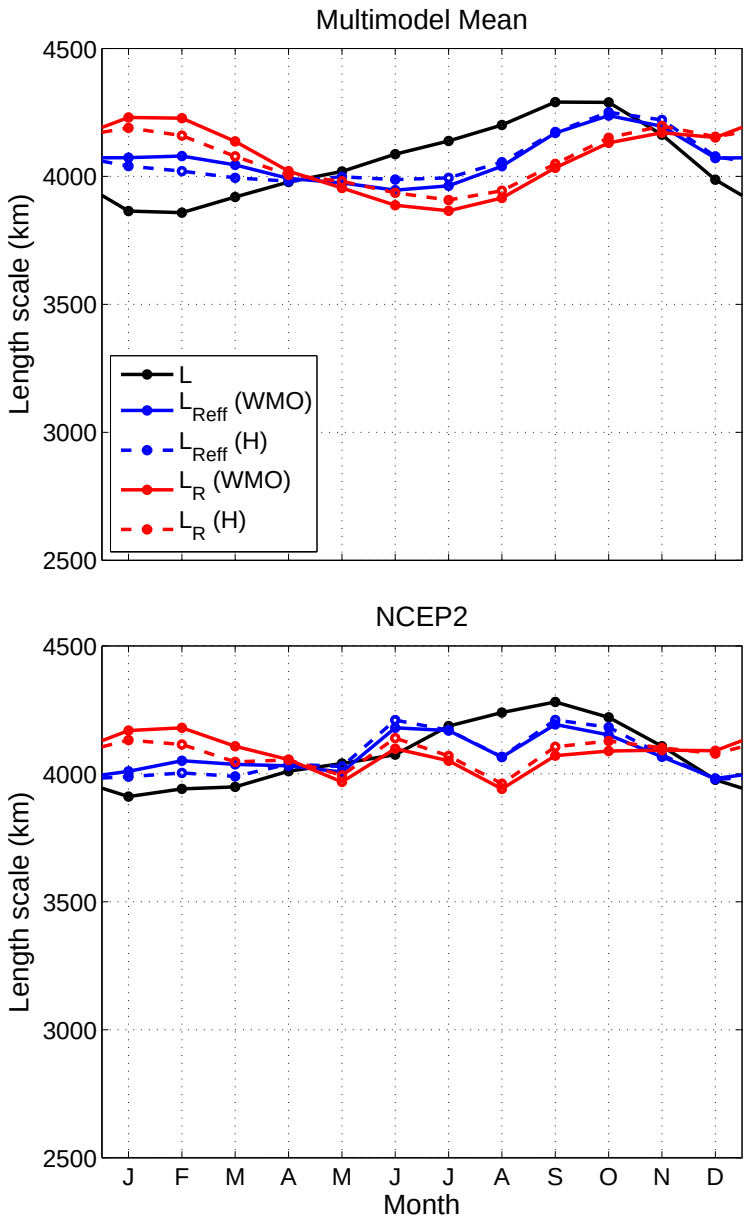

Figure 4-4: Seasonal cycles of eddy length and various dry and effective Rossby radii over 30-70 degrees S during 1981-2000. The Rossby radii labeled (WMO) had the height scale Δp defined as the free troposphere depth, while Rossby radii labeled (H) had Δp identified as the scale height. For all cases f was calculated at the latitude of the maximum in MTT_{eddy}. MTT_{eddy} was evaluated at 850 hPa.

of any Rossby radius seasonal cycle to predict the eddy length seasonal cycle in the southern hemisphere suggests that little is to be learned about the seasonal variation of southern hemisphere eddies by studying corresponding Rossby radii.

Referring to equation 2.4, the dry Rossby radius in any given month i is denoted by

$$L_{Ri} = 2\pi \frac{\langle N^p \Delta p \rangle_i}{f_i} = 2\pi \frac{\langle N^p \rangle_i \langle \Delta p \rangle_i + \langle N^{pa}(\phi) \Delta p^a(\phi) \rangle_i}{f_i}, \tag{4.2}$$

where the departure of a quantity $(\cdot)$ from its regional mean value $\langle (\cdot) \rangle$ is denoted by $(\cdot)^a$.

Because N^p, Δp, and f are all in different units of measure, the monthly variations of these quantities must be written in a nondimensional form to meaningfully compare the contributions of changes in each to the changes in L_R. If for a quantity $(\cdot)$ a monthly anomaly for month i is defined

$$\delta(\cdot)_i = (\cdot)_i - \widehat{(\cdot)}, \tag{4.3}$$

where $\widehat{(\cdot)}$ denotes the annual mean of $(\cdot)$, equation 4.2 can be rewritten

$$L_{Ri} = 2\pi \frac{[\widehat{\langle N^p \rangle} + \delta \langle N^p \rangle_i][\widehat{\langle \Delta p \rangle} + \delta \langle \Delta p \rangle_i]}{\widehat{f}[1 + \delta f_i / \widehat{f}]}, \tag{4.4}$$

where it has been assumed that $\langle N^{pa}(\phi) \Delta p^a(\phi) \rangle_i << \langle N^p \rangle_i \langle \Delta p \rangle_i$ and so the second term in the numerator of equation 4.2 can be dropped.

By additionally assuming that $\left(1 + \delta f_i / \widehat{f}\right)^{-1} \approx 1 - \delta f_i / \widehat{f}$, expanding equation 4.4, and dropping all terms with more than one $\delta(\cdot)_i$ it can be shown that

$$\frac{\delta L_{Ri}}{\widehat{L_R}} = \frac{\delta \langle N^p \rangle_i}{\widehat{\langle N^p \rangle}} + \frac{\delta \langle \Delta p \rangle_i}{\widehat{\langle \Delta p \rangle}} - \frac{\delta f_i}{\widehat{f}}, \tag{4.5}$$

in which all quantities appear in the desired nondimensional form. Equation 4.5 is of course valid for effective Rossby radii as well, when L_R is replaced by L_{Reff} and N^p by N^p_{eff}.

Figs. 4-5 and 4-6 show both sides of equation 4.5 along with each individual

term on the right side of the equation for both dry and effective Rossby radii. The good match between the normalized Rossby radii seasonal cycles and the sum of the seasonal cycles of the components suggests that the approximations made in deriving equation 4.5 are good ones. In view of the results displayed in Figs. 4-1 and 4-2, it is not surprising that very similar results are obtained for both the multimodel mean and NCEP2.

As was previously shown in chapter 3, the effective static stability parameter $\langle N^p_{\text{eff}} \rangle_i$ exhibits a clear seasonal cycle with the maximum in January and the minimum in July. In contrast, the dry static stability parameter $\langle N^p \rangle_i$ has a fractionally much smaller seasonal cycle with maxima in November or December and minima in May or June. The troposphere depth is maximized in August and minimized in February, while the latitude of the maximum in MTT_{eddy} reaches its northern extreme in August and is farthest south in February or March.

The troposphere depth and f evaluation latitude seasonal cycles are of similar amplitude and phased so as to have a tendency to cancel each other out. Because $\langle \Delta p \rangle_i$ is time-independent when Δp is identified as the scale height of the atmosphere, $\delta \langle \Delta p \rangle_i / \widehat{\langle \Delta p \rangle} = 0$ and the cancellation effect disappears. Since $-\delta f_i / \widehat{\langle f \rangle}$ varies roughly in phase with $\langle N^p_{\text{eff}} \rangle_i$ and is considerably larger than the $\langle N^p \rangle_i$ seasonal cycle, the fractional amplitude of rescaled Rossby radius seasonal cycles with Δp identified as the scale height is larger than when Δp is identified as the free troposphere depth. This is consistent with Fig. 4-2.

Finally, it appears that the relatively noisier character of the NCEP2 seasonal cycles as compared to their multimodel mean counterparts, clearly visible in Figs. 4-1 and 4-2, derives mainly from noise in the seasonal cycle of the f evaluation latitude. The relative suppression of this noise in the multimodel mean likely results from the average taken over six GCMs.

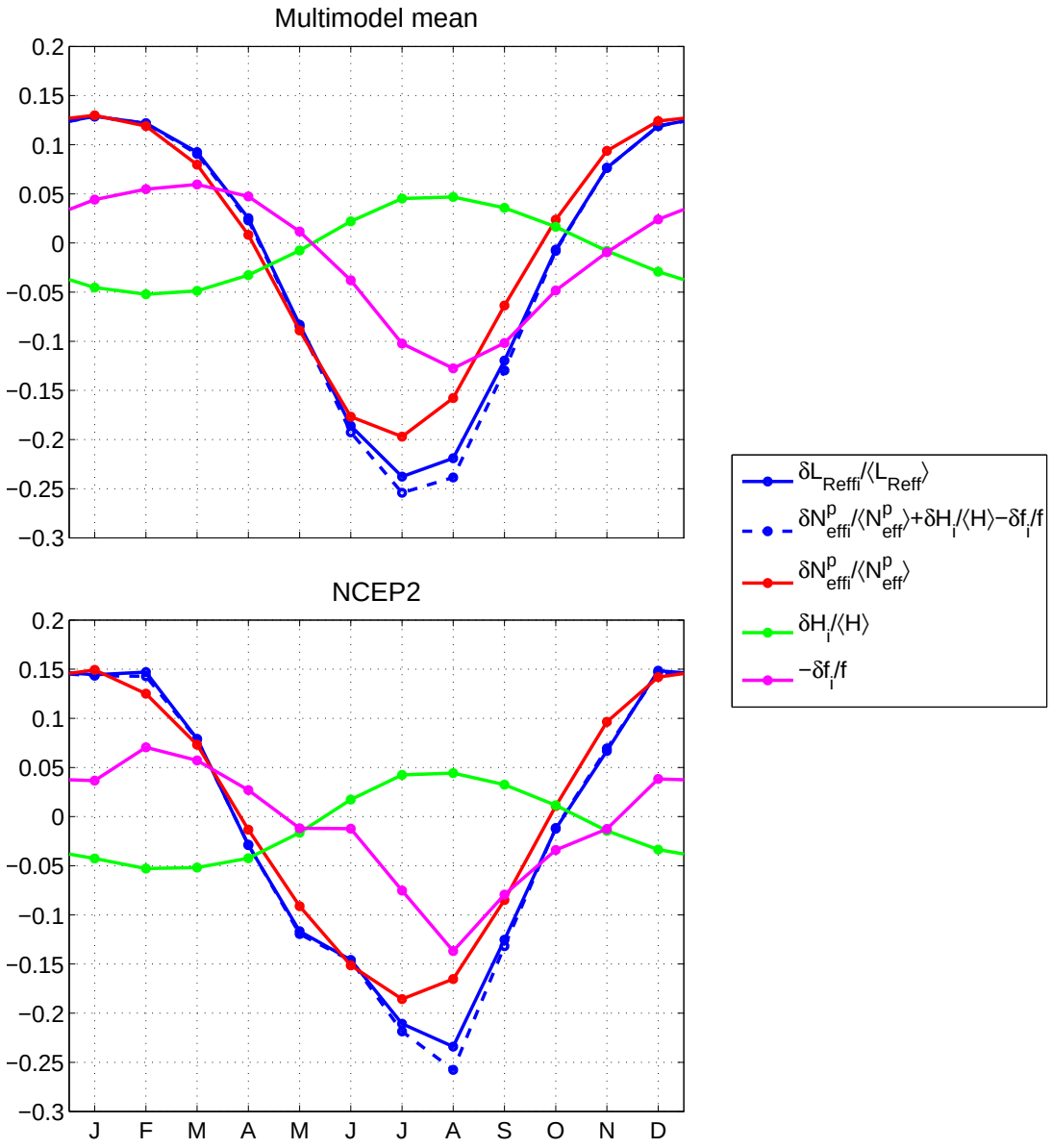

Figure 4-5: Normalized seasonal cycles of L_{Reff}, its components according to equation 4.5, and their sum. f was evaluated at the latitude of the maximum in MTT_{eddy}. Note that the curve associated with the variations of f is actually $-\delta f_i/\widehat{f}$ (the August minimum in $-\delta f_i/\widehat{f}$ is when the latitude of evaluation of f is at its northern extreme and f is maximized). MTT_{eddy} was evaluated at 850 hPa. Hats have been dropped from the text in the legend.

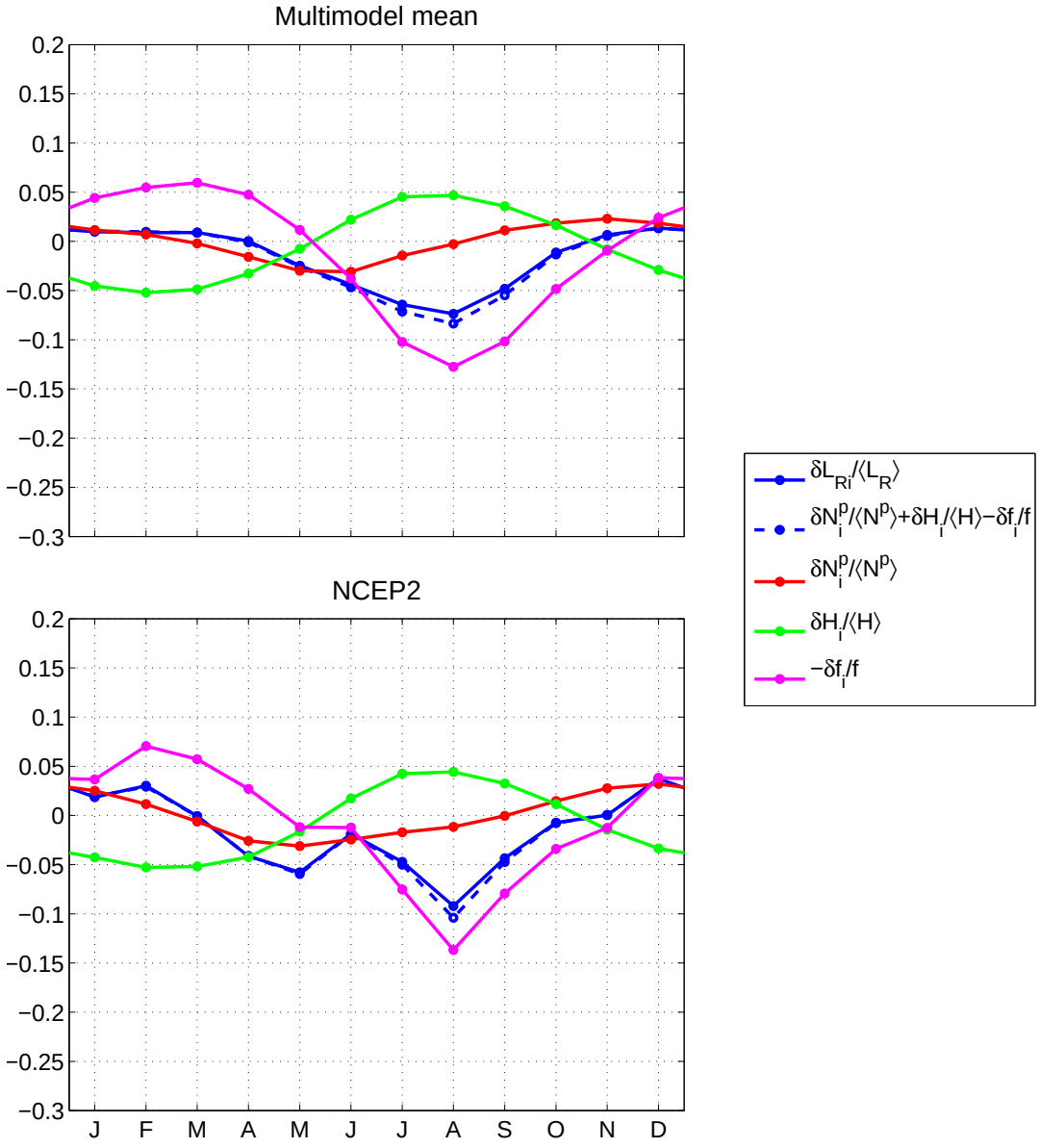

Figure 4-6: Normalized seasonal cycles of L_R, its components, and their sum. Note the greatly reduced amplitude of the N^p seasonal cycle relative to the N^p_{eff} cycle in Fig. 4-5. f was calculated at the latitude of the maximum in MTT_{eddy} and MTT_{eddy} was evaluated at 850 hPa.

Chapter 5

Results–Global Warming

According to Kidston et al. [8], CMIP3 GCMs robustly project an increase in atmospheric eddy lengths over the 21st century. To confirm and further understand this result, annual mean values of the various eddy scales were computed for each of the six GCMs for 1981-2000 and 2081-2100. The GCMs were run for a number of possible emissions scenarios for the 21st century. Only the moderate A1B scenario, in which CO_2 concentrations reach approximately 550 ppm by 2100, is considered here [10]. The annual means were used to compute fractional increases

$$\frac{\delta L_x}{L_x} = \frac{L_x^{21} - L_x^{20}}{L_x^{20}}, \tag{5.1}$$

where L_x^{20} and L_x^{21} denote 1981-2000 and 2081-2100 annual mean eddy scales and $\delta(\cdot)$ now represents the difference between 2081-2100 and 1981-2000 annual means of a quantity $(\cdot)$, instead of a monthly anomaly.

5.1 Multimodel mean

The multimodel mean increases and multimodel mean increases per K of rise in the global mean surface temperature are listed in Table 5.1, along with the multimodel standard deviation to characterize the scatter among the different GCMs. The multimodel mean values of all but one of the eddy scales computed are found to increase

Table 5.1: Multimodel mean fractional increases and fractional increases per K of global mean surface temperature increase are listed for various eddy scales. The increases are calculated using the differences between the 2081-2100 and 1981-2000 means of each eddy scale. For the eddy scale increase per K of temperature increase, the temperature increase is calculated as the difference between the 2081-2100 and 1981-2000 means. The intermodel scatter (one standard deviation) is also given for each quantity. In the first column, (maxMTT) denotes evaluation of f at the latitude of the maximum in MTT_{eddy} and use of the free troposphere depth to define Δp. (meanMTT) indicates evaluation of f at the latitude ϕ_{MTT}, again with the free troposphere depth used to define Δp. Eddy scales marked (H) had f evaluated at the maximum of MTT_{eddy} but used the scale height as Δp. (maxEKE) indicates evaluation of β at the latitude of the maximum in EKE. MTT_{eddy} and ϕ_{MTT} were evaluated at 850 hPa, while EKE was evaluated using winds at 300 hPa.

Length scale		Northern hemisphere increase		Southern hemisphere increase	
		%	% K^{-1}	%	% K^{-1}
L		2.1 ± 0.7	0.78 ± 0.26	4.0 ± 1.4	1.50 ± 0.49
L_R	(maxMTT)	3.8 ± 2.0	1.47 ± 0.83	4.6 ± 1.5	1.73 ± 0.53
L_R	(meanMTT)	5.3 ± 0.9	2.02 ± 0.42	6.0 ± 1.4	2.27 ± 0.52
L_R	(H)	1.3 ± 1.9	0.54 ± 0.73	2.4 ± 1.1	0.91 ± 0.38
L_{Reff}	(maxMTT)	1.2 ± 2.0	0.49 ± 0.78	4.1 ± 2.2	1.54 ± 0.80
L_{Reff}	(meanMTT)	2.7 ± 0.8	1.02 ± 0.41	5.5 ± 2.1	2.07 ± 0.82
L_{Reff}	(H)	-1.4 ± 2.0	-0.46 ± 0.71	1.8 ± 1.8	0.69 ± 0.65
L_β	(maxEKE)	1.6 ± 1.0	0.59 ± 0.42	2.4 ± 1.5	0.89 ± 0.55

between 1981-2000 and 2081-2100. However, in a number of cases the positive value of the increase is within one standard deviation of zero. (The sole decline is also within one standard deviation of zero.)

The multimodel mean eddy scale increases per K of temperature increase are also positive in all but one case, and generally at least one standard deviation above zero. In addition, the multimodel mean of every eddy scale exhibits a larger fractional increase (or smaller fractional decrease) in the southern hemisphere than in the northern hemisphere. But for some individual models and eddy scales, fractional increases are larger in the northern hemisphere.

5.2 Individual GCMs

To further investigate the modeled increases in eddy scales, fractional increases in L are plotted against fractional increases in the various L_R, L_{Reff}, and L_β for each GCM and hemisphere in Figs. 5-1, 5-2, and 5-3. The eddy length and Rhines scale are found to increase for all models and hemispheres, as do the dry Rossby radii for all but one combination of model, hemisphere, and f evaluation latitude/Δp. The effective Rossby radii results are more complex, with the choice of the scale height rather than the free troposphere depth for Δp clearly reducing values of $\delta L_{\mathrm{Reff}}/L_{\mathrm{Reff}}$. For four of the six GCMs, northern hemisphere values of L_{Reff} calculated with the scale height as Δp are in fact projected to decline over the 21st century.

Although the changes are positive for most models, hemispheres, and eddy scales, they nevertheless vary considerably among GCMs. Using a method similar to that in [8], if it is assumed that the fractional increase in eddy length $\delta L/L$ for each model is perfectly explained by the fractional increase in one of the other eddy scales $\delta L_x/L_x$, the points $(\delta L_x/L_x, \delta L/L)$ for all six GCMs should fall on the line $\delta L/L = \delta L_x/L_x$. Accordingly, analysis of the intermodel scatter in values of the fractional increases in the eddy length, the Rossby radii, and the Rhines scale could yield insight into the causes of the modeled eddy length increase.

Inspection of Figs. 5-1, 5-2, and 5-3 indicates that the simple ideal of a clear $\delta L/L = \delta L_x/L_x$ for a single L_x does not describe the behavior of the GCMs. For all of the L_x studied, the southern hemisphere values of $\delta L/L$ do generally increase with increasing $\delta L_x/L_x$. However, $\delta L/L$ can be systematically underestimated (as by $\delta L_{\mathrm{Reff}}/L_{\mathrm{Reff}}$ with f at the maximum in MTT_{eddy} and the scale height as Δp) or overestimated (as by $\delta L_R/L_R$ with f evaluated at ϕ_{MTT} and the free troposphere depth as Δp). This roughly monotonic relationship between $\delta L/L$ and $\delta L_x/L_x$ does not carry over to the northern hemisphere. Instead, $(\delta L_x/L_x, \delta L/L)$ points form clumps or spread out over larger ranges in $\delta L_x/L_x$ than in $\delta L/L$.

To quantify the quality of the fit of a set of $(\delta L_x/L_x, \delta L/L)$ points to a hypothe-

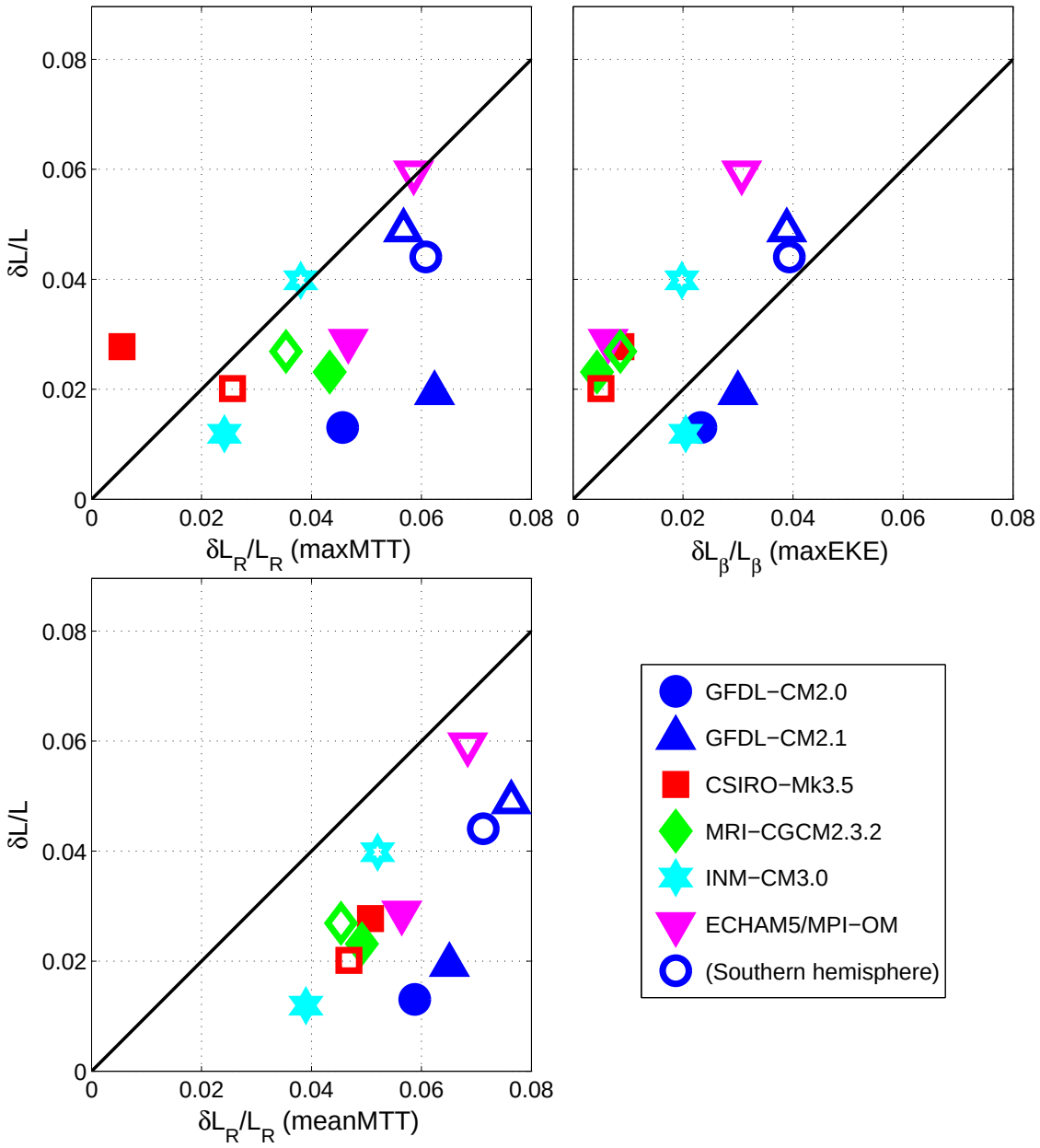

Figure 5-1: Scatterplots of fractional changes in eddy length L compared to fractional changes in the dry Rossby radii L_R with f evaluated at the latitude of the maximum in MTT_{eddy} (maxMTT, upper left panel) or at the characteristic latitude ϕ_{MTT} (meanMTT, lower left panel). For both dry Rossby radii, Δp was identified as the free troposphere depth. The upper right panel displays the fractional change in eddy length L compared to the fractional change in the Rhines scale L_β with β evaluated at the latitude of the maximum in EKE. MTT_{eddy} and ϕ_{MTT} were evaluated at 850 hPa, and EKE was calculated using winds at 300 hPa.

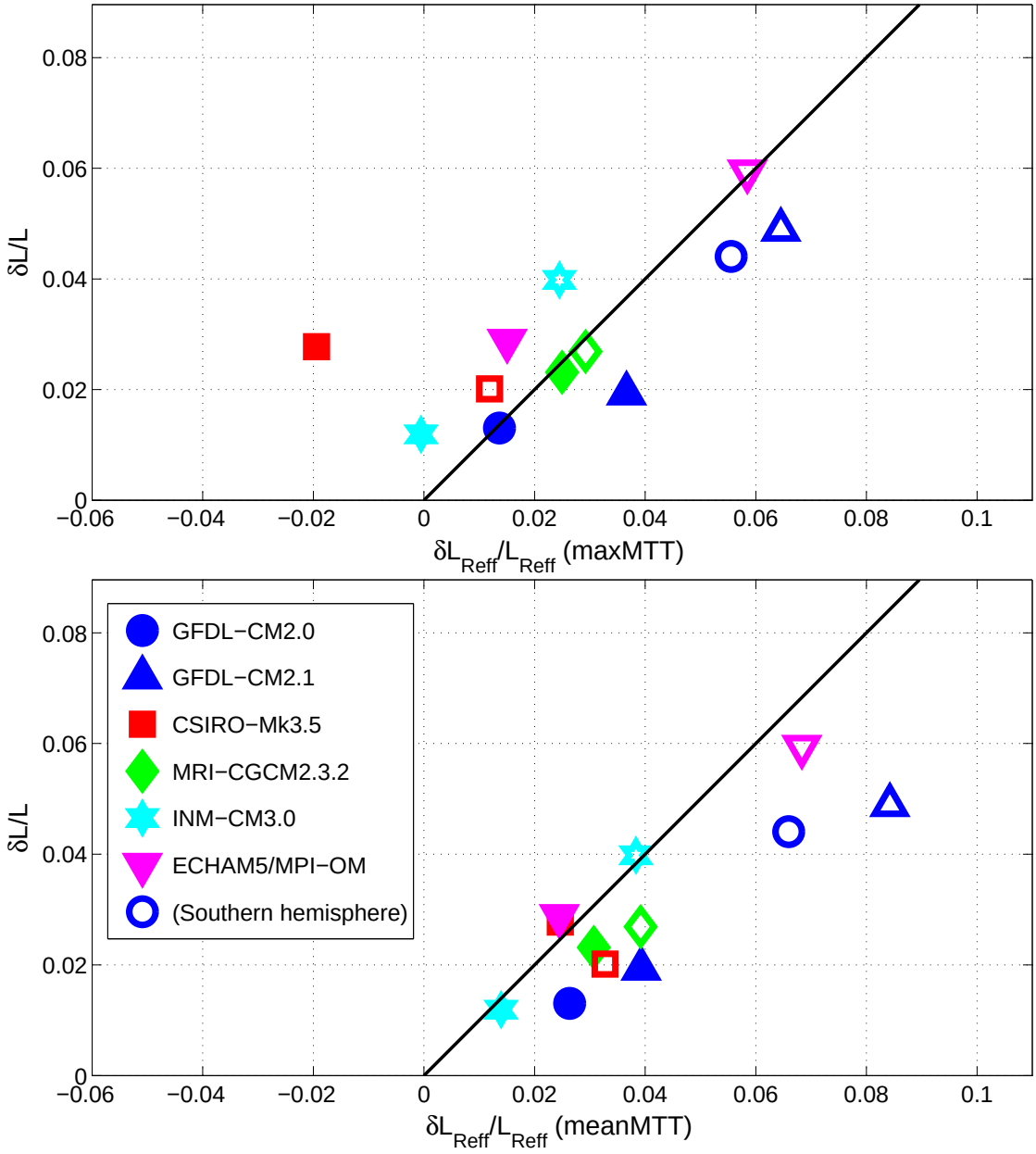

Figure 5-2: Scatterplots of fractional changes in eddy length L compared to fractional changes in the effective Rossby radii L_{Reff} with f evaluated at the latitude of the maximum in MTT_{eddy} (maxMTT, upper panel) or at the characteristic latitude ϕ_{MTT} (meanMTT, lower panel). MTT_{eddy} and ϕ_{MTT} were calculated at 850 hPa, and in both cases the free troposphere depth was used as Δp.

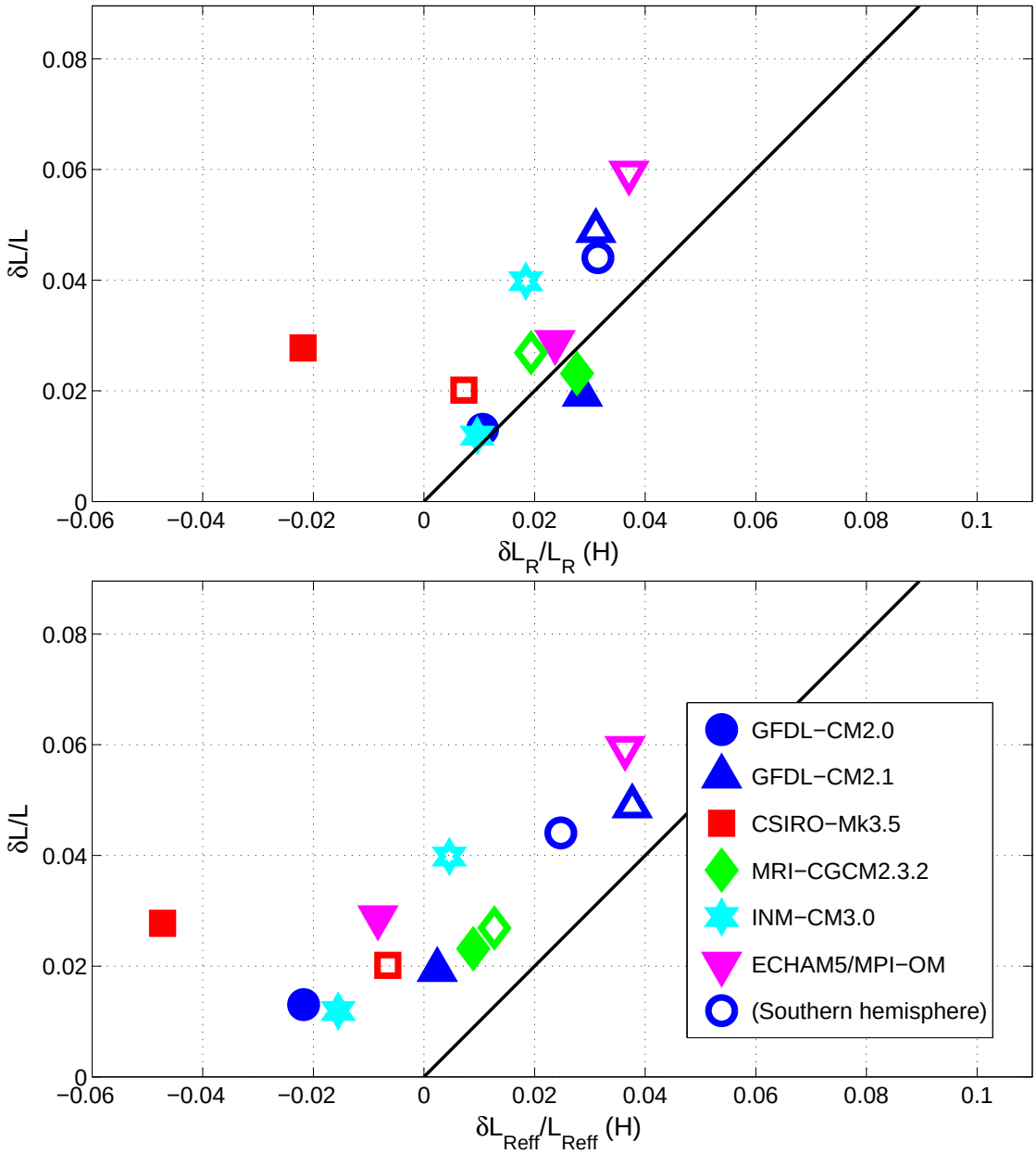

Figure 5-3: Scatterplots of fractional changes in eddy length L compared to fractional changes in L_R and L_{Reff} with f evaluated at the latitude of the maximum in MTT_{eddy}. Unlike in Figs. 5-1 and 5-2, Δp was identified as the scale height. MTT_{eddy} was evaluated at 850 hPa.

sized line $\delta L/L = \delta L_x/L_x$, an error parameter E will be defined

$$E = \left(\frac{1}{n} \sum_{i=1}^{n} \left[\left(\frac{\delta L}{L} \right)^i - \left(\frac{\delta L_x}{L_x} \right)^i \right]^2 \right)^{1/2}, \tag{5.2}$$

where i indexes over the n $(\delta L_x/L_x, \delta L/L)$ points. E is the RMS value of the difference between an actual eddy length increase $\delta L/L$ and the increase of another eddy scale $\delta L_x/L_x$. $\delta L_x/L_x$ is regarded as a prediction of $\delta L/L$, and so lower values of E indicate a more successful prediction. E can be calculated for $(\delta L_x/L_x, \delta L/L)$ values from a single hemisphere, or for both hemispheres simultaneously. In the former case, i is indexing over the different GCMs and so $n = 6$. In the latter case, i indexes over both GCMs and hemispheres and thus $n = 12$.

E was computed separately in each hemisphere and for both hemispheres together, and the results are displayed in Table 5.2. The patterns of E values are different in each hemisphere. The lowest value of E in the southern hemisphere is associated with one of the dry Rossby radii, but both L_R and L_{Reff} with f evaluated at the latitude of the maximum in MTT_{eddy} and the free troposphere depth as Δp are substantially better fits than the other four Rossby radii. Evidently the southern hemisphere results are more sensitive to the choices of f evaluation latitude and Δp than to the choice of dry or effective static stability parameter. In the northern hemisphere and the global mean, two of the three versions of L_{Reff} yield lower values of E than their L_R counterparts. But when the scale height is used for Δp, L_R is a better fit than L_{Reff} and the value of E for the northern hemisphere L_{Reff} is the largest value of E in either hemisphere.

In view of the complex results described above, it must be concluded that diagnosis of the changes in dry and effective Rossby radii and the Rhines scale does not supply an unambiguous explanation of the cause of the modeled increase in eddy length. If the eddy length is indeed set by a characteristic scale of baroclinic instability, changes in L_{Reff} should supply an explanation of eddy length changes that is superior to the explanation provided by changes in L_R. This is because, as discussed in chapter 3,

the former quantity is a better representation of the relevant physics.

While this hypothesized superiority is not clearly established, it can at least be reconciled with the analysis presented. Although the change in southern hemisphere eddy lengths was best explained by changes in one of the dry Rossby radii, the relative sensitivity of the E_S values to the methods of selecting f and Δp suggests that the changes in N^p and N^p_{eff} are very similar in the southern hemisphere. This possibility is consistent with L_{Reff}, with f evaluated at the maximum in MTT_{eddy} and the free troposphere depth as Δp, being the quantity that is truly physically relevant in determining the southern hemisphere eddy length.

In the northern hemisphere, if the free troposphere depth is taken as the correct choice of Δp the E_N values for L_{Reff} are consistently lower than those for L_R. This is also consistent with the eddy length being set by L_{Reff} with f evaluated at the maximum in MTT_{eddy} and the free troposphere depth as Δp. However, the single lowest value of E_N is in fact associated with L_{Reff} with f evaluated at ϕ_{MTT}. If Δp is actually the scale height, L_R is a better fit than L_{Reff} in both hemispheres. In neither hemisphere is it possible to dismiss L_β as the control on eddy length.

Table 5.2: Values of the error parameter E defined in equation 5.2 are listed for each hemisphere individually and both combined. (maxMTT) denotes evaluation of f at the latitude of the maximum in MTT_{eddy}, while (meanMTT) indicates evaluation of f at the latitude ϕ_{MTT}. Δp was taken as the free troposphere depth for both the (maxMTT) and (meanMTT) cases. For the (H) cases, f was again evaluated at the latitude of the maximum in MTT_{eddy} but the scale height was used as Δp. (maxEKE) indicates β evaluation at the latitude of the maximum in EKE. MTT_{eddy} and ϕ_{MTT} were calculated at 850 hPa, while EKE was calculated using 300 hPa winds.

Eddy scale L_x		E_N (Northern hemisphere)	E_S (Southern hemisphere)	E_B (Both hemispheres)
L_R	(maxMTT)	0.027	0.009	0.020
L_R	(meanMTT)	0.034	0.022	0.028
L_R	(H)	0.021	0.017	0.019
L_{Reff}	(maxMTT)	0.022	0.011	0.017
L_{Reff}	(meanMTT)	0.011	0.019	0.015
L_{Reff}	(H)	0.040	0.023	0.032
L_β	(maxEKE)	0.016	0.018	0.017

Chapter 6

Conclusion

This thesis presents an analysis of the variations in atmospheric eddy length exhibited by six GCMs and the NCEP2 reanalysis. The seasonal cycle of eddy length in the 20th century climate is determined and compared with the seasonal cycles in other length scales hypothesized to control the eddy length, including a recently-developed modification of the Rossby radius that attempts to account for the influence of latent heating on the dynamics of the eddies. The latent heating is parameterized as a modification to the static stability, to create a new effective static stability. The modification depends in part on the value of a parameter λ, which characterizes the asymmetry in vertical wind velocity fields. The value of λ is found not to vary significantly with the seasons, making it easy to calculate the effective static stability.

GCM-simulated seasonal cycles of the eddy length and other eddy scales are similar to those seen in the NCEP2 reanalysis. The GCMs are also used to study changes in annual mean eddy scales with global warming, and are found to project an increase in the eddy length. The increase in eddy lengths is seen in both hemispheres of all six GCMs.

In the northern hemisphere, eddy lengths peak in the winter and are minimized during the summer. This qualitative behavior is reproduced by both the effective Rossby radius L_{Reff}, which incorporates the effects of latent heating, and the Rhines scale L_β. However, the Rhines scale is too constant during the winter.

The traditional dry Rossby radius L_R, which neglects latent heating, is a weaker

explanation of the northern hemisphere eddy length seasonal cycle if Δp is taken as the free troposphere depth. Although L_R is smaller in summer than in winter, its seasonality is less than that of the eddies. The substantial difference between the seasonal cycles of L_R and the effective Rossby radius L_{Reff}, which incorporates the latent heating effect, results from the seasonal cycle of the effective static stability parameter $\langle N^p_{\mathrm{eff}} \rangle$ having a much larger amplitude than the dry static stability parameter $\langle N^p \rangle$. The annual mean value of $\langle N^p_{\mathrm{eff}} \rangle$ is also significantly lower than the annual mean $\langle N^p \rangle$.

Although the author is unaware of any previous work directly addressing the seasonal cycle of the eddy length or other relevant eddy scales, Valdes and Hoskins (1988) [21] conducted linear stability analyses of the seasonally varying mean flow of the Earth's atmosphere. Plots of the growth rates of waves of different zonal wavenumbers (their Figs. 2 and 5) suggest that the maximum in the growth rate occurs at slightly lower zonal wavenumber (longer zonal wavelength) in the northern hemisphere winter. Valdes and Hoskins made no attempt to incorporate latent heating in their study. If the result of Merlis and Schneider [11] is accepted that the length scale of the most rapidly growing linear wave is explained by the Rossby radius is accepted, the Valdes and Hoskins results imply that the northern hemisphere dry Rossby radius should be longer in winter than in summer. Such a seasonal dependence is indeed found in the present study.

The southern hemisphere seasonal cycle results are more difficult to understand and have not been satisfactorily explained. The eddy length seasonal cycles observed in the reanalysis and simulated by the GCMs are in reasonable agreement, suggesting that the GCMs correctly represent whatever processes set the eddy length, but no Rossby radius or Rhines scale seasonal cycle reproduces the eddy length seasonal cycle.

While a conclusive explanation of this behavior is not currently available, one possibility will be briefly described. The Valdes and Hoskins study [21] explored the effect of topography on the instability by comparing linear stability analyses in which the Earth's surface was taken as flat to analyses with zonally-averaged orography. In

the case with orography, the growth rate maximum of the linear waves moves to a larger zonal wavelength in the southern hemisphere winter. This is consistent with the seasonality of the southern hemisphere eddy length as determined in the present work, but inconsistent with the the seasonality of the multimodel mean dry Rossby radii. (The NCEP2 results are more ambiguous, as shown in Figs. 4-3 and 4-4.)

One possible interpretation of this state of affairs is that the relationship between the (dry) Rossby radius and the zonal wavelength of (dry) growing linear waves found in the idealized GCM of Merlis and Schneider [11] breaks down in the southern hemisphere of the real Earth and more realistic GCMs. If it is then posited that the zonal wavelength of the fastest growing wave in a dry linear stability analysis explains the eddy lengths seen in the atmosphere and in moist GCMs, it may be possible to correctly predict the seasonality of the southern hemisphere eddy length. This scenario does not explain why the results of a dry stability analysis would be valid in the moist atmosphere. But the seasonality of both $\langle N^p \rangle$ and $\langle N^p_{\text{eff}} \rangle$ is much weaker in the southern hemisphere than in the northern hemisphere (Fig. 3-2), so the difference between the two static stability parameters may get lost in the proportionality constant relating the wavelength of the most rapidly growing linear wave to the eddy length.

A possible source of the breakdown in the relationship between the linearly most unstable wave and the eddy length is suggested by the Phillips model of baroclinic instability (J. Kidston, pers. comm.). The Phillips model exhibits a dependence of the growth rate of baroclinic waves not only on the Rossby radius but also on the vertical shear of the flow. Increasing vertical shear results in an increase in the wavelength of the most unstable wave [22]. In the atmosphere, the midlatitude jets are strongest in the winter, which corresponds to an increase in vertical shear [9].

Taking either the dry or the effective Rossby radius as an initial estimate of the scale of the most unstable linear waves in the atmosphere, this suggests that an improved estimate of the scale of the waves would revise the winter values upward and the summer values downward. Inspection of Figs. 4-3 and 4-4 suggests that such a correction would result in better agreement between the seasonal cycles of the estimated scale of the fastest growing linear wave and the eddy length, consistent with

the hypothesis that the eddy length is set by the scale of the fastest growing linear wave. However, the same correction applied to the northern hemisphere seasonal cycle of the effective Rossby radius (to bring it closer to the seasonal cycle of the zonal wavelength of the fastest growing linear wave) would worsen its agreement with the eddy length seasonal cycle.

Finally, annual means of the eddy length, Rossby radii, and Rhines scale were calculated for each GCM for the years 1981-2000 and 2081-2100. As the climate warms, eddy lengths are found to increase in every GCM and hemisphere. This is consistent with the results of Kidston et al., even though the GCM experiments in the present study had weaker radiative forcing than in Kidston et al. [8, 10]. The eddy length increased more in the southern hemisphere than in the northern hemisphere for every GCM but CSIRO-Mk3.5, a pattern that also exists in Kidston et al.'s analyses of the six GCMs used in this study.

The various dry and effective Rossby radii and the Rhines scale were also found to generally increase with global warming. The most prominent exception to this trend was the northern hemisphere effective Rossby radius evaluated with Δp as the scale height, which declined for four of the six GCMs. The fractional changes in the Rossby radii and Rhines scale can be construed as predictions of the fractional change in the eddy length, and using this idea a method of quantitatively assessing the correctness of the predictions was presented. The results of this assessment do not clearly identify a single eddy scale as having unique success in the predicting the changes in eddy length, so exactly which eddy scale (if any of them) sets the eddy length is still unclear. However, the success of the GCMs in reproducing the eddy length seasonal cycle of the NCEP2 reanalysis and the fact that Rossby radii still generally increase over the 21st century when latent heating is taken into account increases confidence in Kidston et al.'s finding that eddy lengths are likely to increase with global warming.

Several extensions of the present work are possible. First, an attempt could be made to incorporate additional CMIP3 GCMs in the analysis. Output from more than 20 GCMs was contributed to the CMIP3 archive. Not all of them have the

necessary data available, but an exhaustive search of the archive to ensure that all GCMs with adequate data are included in the analysis has not been performed. Second, the availability of the new CMIP5 archive presents several opportunities for analyses not possible with the CMIP3 dataset. Daily mean values of ω are to be archived for some of the CMIP5 experiments, permitting direct calculation of λ and facilitating studies of possible future changes [19]. Additionally, the CMIP5 experimental program includes simulations of the last glacial maximum and the mid-Holocene [20]. In conjunction with the simulations of future warming, these could be used to study the variability of eddy length across a broader range of climates. However, the eddy length and the Rhines scale would need to be calculated from six-hourly instantaneous winds instead of the daily-mean winds used in the present work [19].

Bibliography

[1] L. Barry, G. C. Craig, and J. Thuburn. Poleward heat transport by the atmospheric heat engine. *Nature*, 415:774–777, 2002. doi:10.1038/415774a.

[2] J. G. Charney. The dynamics of long waves in a baroclinic westerly current. *J. Meteor.*, 4:135–162, 1947.

[3] E. T. Eady. Long waves and cyclone waves. *Tellus*, 1:33–52, 1949.

[4] K. A. Emanuel, M. Fantini, and A. J. Thorpe. Baroclinic instability in an environment of small stability to slantwise moist convection. Part I: Two-dimensional models. *J. Atmos. Sci.*, 44:1559–1573, 1987.

[5] M. Fantini. Nongeostrophic corrections to the eigensolutions of a moist baroclinic instability problem. *J. Atmos. Sci.*, 47:1277–1287, 1990.

[6] D. M. W. Frierson, I. M. Held, and P. Zurita-Gotor. A gray-radiation aquaplanet moist GCM. Part I: Static stability and eddy scale. *J. Atmos. Sci.*, 63:2548–2566, 2006. doi:10.1175/JAS3753.1.

[7] M. Kanamitsu, W. Ebisuzaki, J. Woollen, S. K. Yang, J. J. Hnilo, M. Fiorino, and G. L. Potter. NCEP–DOE AMIP-II Reanalysis (R-2). *Bull. Amer. Meteor. Soc.*, 83:1631–1643, 2002. doi:10.1175/BAMS-83-11-1631.

[8] J. Kidston, S. M. Dean, J. A. Renwick, and G. K. Vallis. A robust increase in the eddy length scale in the simulation of future climates. *Geophys. Res. Lett.*, 37:L03806, 2010. doi:10.1029/2009GL041615.

[9] J. Marshall and R. A. Plumb. *Atmosphere, Ocean, and Climate Dynamics: An Introductory Text*. Elsevier Academic Press, Boston, 2008.

[10] G. A. Meehl, C. Covey, K. E. Taylor, T. Delworth, R. J. Stouffer, M. Latif, B. McAvaney, and J. F. B. Mitchell. The WCRP CMIP3 Multimodel Dataset: A New Era in Climate Change Research. *Bull. Amer. Meteor. Soc.*, 88:1383–1394, 2007. doi:10.1175/BAMS-88-9-1383.

[11] T. M. Merlis and T. Schneider. Scales of linear baroclinic instability and macroturbulence in dry atmospheres. *J. Atmos. Sci.*, 66:1821–1833, 2009. doi:10.1175/2008JAS2884.1.

[12] P. A. O'Gorman. The effective static stability experienced by eddies in a moist atmosphere. *J. Atmos. Sci.*, 68:75–90, 2011. doi:10.1175/2010JAS3537.1.

[13] J. Pedlosky. *Geophysical Fluid Dynamics*. Springer-Verlag, New York, second edition, 1987.

[14] N. A. Phillips. Energy transformations and meridional circulations associated with simple baroclinic waves in a two-level, quasi-geostrophic model. *Tellus*, 6:273–286, 1954.

[15] T. Reichler, M. Dameris, and R. Sausen. Determining the tropopause height from gridded data. *Geophys. Res. Lett.*, 30:2042, 2003. doi:10.1029/2003GL018240.

[16] P. B. Rhines. Waves and turbulence on a beta-plane. *J. Fluid Mech.*, 69:417–443, 1975.

[17] T. Schneider, P. A. O'Gorman, and X. J. Levine. Water vapor and the dynamics of climate changes. *Rev. Geophys.*, 48:RG3001, 2010. doi:10.1029/2009RG000302.

[18] T. Schneider and C. C. Walker. Self-organization of atmospheric macroturbulence into critical states of weak nonlinear eddy-eddy interactions. *J. Atmos. Sci.*, 63:1569–1586, 2006. doi:10.1175/JAS3699.1.

[19] K. Taylor. Listed of requested output for CMIP5, April 2011. Available at `http://cmip-pcmdi.llnl.gov/cmip5/output_req.html#req_format`, accessed 7 May 2011.

[20] K. E. Taylor, R. J. Stouffer, and G. A. Meehl. A summary of the CMIP5 experiment design, January 2011. Available at `http://cmip-pcmdi.llnl.gov/cmip5/experiment_design.html?submenuheader=1`, accessed 7 May 2011.

[21] P. J. Valdes and B. J. Hoskins. Baroclinic instability of the zonally averaged flow with boundary layer damping. *J. Atmos. Sci.*, 45:1584–1593, 1988.

[22] G. K. Vallis. *Atmospheric and Oceanic Fluid Dynamics: Fundamentals and Large-Scale Circulation*. Cambridge University Press, Cambridge, 2006.

[23] G. K. Vallis and M. E. Maltrud. Generation of mean flows and jets on a beta-plane and over topography. *J. Phys. Ocean.*, 23:1346–1362, 1993.

[24] P. Zurita-Gotor. Updraft/downdraft constraints for moist baroclinic modes and their implications for the short-wave cutoff and maximum growth rate. *J. Atmos. Sci.*, 62:4450–4458, 2005.